

Testing the accuracy of microstructure reconstruction in three dimensions using phantoms

This article has been downloaded from IOPscience. Please scroll down to see the full text article.

2012 Modelling Simul. Mater. Sci. Eng. 20 075005

(<http://iopscience.iop.org/0965-0393/20/7/075005>)

View [the table of contents for this issue](#), or go to the [journal homepage](#) for more

Download details:

IP Address: 131.84.11.215

The article was downloaded on 12/09/2012 at 14:41

Please note that [terms and conditions apply](#).

Report Documentation Page

Form Approved
OMB No. 0704-0188

Public reporting burden for the collection of information is estimated to average 1 hour per response, including the time for reviewing instructions, searching existing data sources, gathering and maintaining the data needed, and completing and reviewing the collection of information. Send comments regarding this burden estimate or any other aspect of this collection of information, including suggestions for reducing this burden, to Washington Headquarters Services, Directorate for Information Operations and Reports, 1215 Jefferson Davis Highway, Suite 1204, Arlington VA 22202-4302. Respondents should be aware that notwithstanding any other provision of law, no person shall be subject to a penalty for failing to comply with a collection of information if it does not display a currently valid OMB control number.

1. REPORT DATE 05 SEP 2012		2. REPORT TYPE		3. DATES COVERED 00-00-2012 to 00-00-2012	
4. TITLE AND SUBTITLE Testing The Accuracy Of Microstructure Reconstruction In Three Dimensions Using Phantoms				5a. CONTRACT NUMBER	
				5b. GRANT NUMBER	
				5c. PROGRAM ELEMENT NUMBER	
6. AUTHOR(S)				5d. PROJECT NUMBER	
				5e. TASK NUMBER	
				5f. WORK UNIT NUMBER	
7. PERFORMING ORGANIZATION NAME(S) AND ADDRESS(ES) Carnegie Mellon University, Department of Materials Science and Engineering, 5000 Forbes Ave, Pittsburgh, PA, 15213				8. PERFORMING ORGANIZATION REPORT NUMBER	
9. SPONSORING/MONITORING AGENCY NAME(S) AND ADDRESS(ES)				10. SPONSOR/MONITOR'S ACRONYM(S)	
				11. SPONSOR/MONITOR'S REPORT NUMBER(S)	
12. DISTRIBUTION/AVAILABILITY STATEMENT Approved for public release; distribution unlimited					
13. SUPPLEMENTARY NOTES MODELLING AND SIMULATION IN MATERIALS SCIENCE AND ENGINEERING, vol 20 (2012), Published 5 September 2012, Government or Federal Purpose Rights License					
14. ABSTRACT Three-dimensional (3D) multi-region explicit geometric modeling of implicit images of polycrystalline materials microstructure is tested for accuracy and fitness using 3D Phantom geometries. Implicit data sets are generated from the explicit phantoms by sampling the phantoms over a range of resolutions from which explicit representations are then reconstructed. The reconstructed models are tested for error against the phantoms to characterize the accuracy of the reconstruction techniques as a function of resolution. The error of the reconstructed geometries decreases with increasing resolution. However the mean width of the reconstructed regions are consistently lower than the phantoms.					
15. SUBJECT TERMS					
16. SECURITY CLASSIFICATION OF:			17. LIMITATION OF ABSTRACT	18. NUMBER OF PAGES	19a. NAME OF RESPONSIBLE PERSON
a. REPORT unclassified	b. ABSTRACT unclassified	c. THIS PAGE unclassified			

Testing the accuracy of microstructure reconstruction in three dimensions using phantoms

S D Sintay¹ and A D Rollett²

¹ IAT-3, Los Alamos National Laboratory, MS C937, NM 87545, USA

² Department of Materials Science and Engineering, Carnegie Mellon University, 5000 Forbes Ave, Pittsburgh, PA 15213, USA

E-mail: ssintay@lanl.gov and rollet@andrew.cmu.edu

Received 2 March 2012, in final form 25 July 2012

Published 5 September 2012

Online at stacks.iop.org/MSMSE/20/075005

Abstract

Three-dimensional (3D) multi-region explicit geometric modeling of implicit images of polycrystalline materials microstructure is tested for accuracy and fitness using 3D Phantom geometries. Implicit data sets are generated from the explicit phantoms by sampling the phantoms over a range of resolutions, from which explicit representations are then reconstructed. The reconstructed models are tested for error against the phantoms to characterize the accuracy of the reconstruction techniques as a function of resolution. The error of the reconstructed geometries decreases with increasing resolution. However, the mean width of the reconstructed regions are consistently lower than the phantoms.

(Some figures may appear in colour only in the online journal)

1. Introduction

Reconstruction of three-dimensional (3D) objects based on image density data is the object of intense research and commercial implementation [3, 11, 12, 25]. Less common and less well developed are the analysis and reconstruction of multi-material images. Polycrystalline materials as routinely encountered in metals and ceramics fall into the multi-material category where image segmentation is often aided by the availability of data on crystallographic orientation [21]. There remains, however, the challenge of developing algorithms to generate explicit representations of the internal interfaces such as the grain boundary networks. These features control many aspects of materials behavior and performance [26]. The tools to be applied in this work are drawn from the practice of computational geometry for which there is a small but growing body of examples of its application in materials science [8].

Physical proxies or phantoms play a prominent role in quality assurance and quality control factors in non-destructive medical imaging [10]. In the simplest description, phantoms are 3D

objects that have been engineered to replicate the response of humans and they are used in place of humans during the testing of medical imaging devices. They provide a ground truth or standard whereby the imaging hardware and reconstruction software can be tested for accuracy and repeatability. The American Association of Physicists in Medicine (AAPM) drafted and accepted a phantom-based protocol for specifications and quality assurance methods in magnetic resonance imaging (MRI) scanners [19]. As new imaging techniques and apparatus are developed, suitable new physical phantoms are developed leading to the adoption of new standards [6, 9, 32]. Physical phantoms provide a stable, repeatable means to collect data on existing tomographic systems and they have the advantage that they provide real world conditions to test hardware and software advances. The disadvantages are that they are limited in complexity, they are not easily reconfigurable to test emerging imaging needs, and these are often not realistic. Even with these limitations, physical phantoms are extremely useful and play a prominent role in the science and technology of 3D medical imaging. The materials science community has only recently begun to consider the value of phantoms, and no physical phantoms are known to exist for polycrystalline materials.

Where physical phantoms are not available, digital phantoms excel. A digital phantom is a simulated representation of a 3D object. They are highly reconfigurable and can be extremely complex and realistic. Two prominent projects related to creating digital phantoms in the medical imaging community are the *Brainweb: Simulated Brain Database* [7] and *The Visible Human Project* [17, 20]. Digital phantoms are a gold standard because they can be defined to whatever numerical accuracy is available and enable objective evaluation of digital image processing techniques. They allow quantitative analysis of the reconstruction algorithms and through their adaptability the performance of an algorithm can be evaluated under a wide range of conditions (e.g. changes in resolution, noise, drift, low signal intensity, etc) [18, 25]. One of the foci of this paper is the use of digital phantoms to represent polycrystalline materials.

A space filling aggregate of grains is a close packed assembly of geometric objects that yield a non-manifold interface structure. When two regions intersect, a 3D surface is defined; when three (or more in the special case of the ‘checker board’ arrangement) regions intersect, a 3D space curve is defined; and when four (with the exception of the special case) or more regions intersect a point is defined. In a polycrystalline material these are commonly referred to as grain boundaries, triple lines and quadruple points, respectively. Alternatively, these topological entities are also referred to as patches (grain boundaries), edges (triple lines) and corners (quad points or nodes) [2]³.

The complete non-manifold interface geometry (grain boundary network) can also be represented by the union of many ‘2-manifold surfaces with edge’⁴. In this case, each grain boundary would be a 2-manifold surface with edge, the triple line would be the joining of three (or more) 2-manifold surfaces, and the quad point would be a singular point at the intersection of four 2-manifold surfaces. At the micrometer length scale it is reasonable to assume that the surfaces and lines are continuous geometric features with continuous curvatures, i.e. steps, kinks and holes are not expected to exist as real features of grain boundaries and triple lines when no topology changes occur⁵.

Observed and reconstructed microstructures are typically represented in the format of standard images, and many physics-based microstructure modeling strategies are also commonly implemented on regular grids in two dimensions and three dimensions [5, 22]. This

³ The special case of four or more grains forming a line in three dimensions is thermodynamically unstable for boundaries of uniform energy and in real microstructures it is generally not observed.

⁴ The phrase ‘2-manifold surface with edge’ is used to delineate a surface that is 2-manifold but is that bounded on all sides by an edge such that it is not infinite.

⁵ At the mesoscale we neglect the atomic structure of solids.

regular discrete arrangement of microstructure data means that the core geometric features of the grain boundary interface network, i.e. grain boundaries, triple lines and quad points, are implicitly defined through pixels or voxels. The complex topology and topological changes within a microstructure present some unique challenges to extracting an explicit geometric representation of the data.

The topological and interface mapping challenges for multi-material implicit data sets are well understood [1, 14, 15, 23]. Wang [31] provides a good review of the many approaches to iso-surface extraction for both binary and multi-material data. His review includes progress in marching cubes, dual grid contouring, active deformation approaches and their variants.

The goal of this paper is to test the accuracy of a geometry extraction algorithm on a series of 3D images generated from digital phantoms of polycrystalline materials. Two phantoms, 9 and 41 regions respectively, are prepared, sampled and then explicit representations reconstructed using a dual grid based algorithm [27]. The accuracy of various features of the reconstructions are determined by comparing the phantoms with the reconstructed geometries.

2. Procedure

The value of a digital phantom is its ability to accurately represent microstructure features of interest in a digital format. When grains, grain boundaries, inclusions, voids, precipitate phases, etc are considered it is clear that creating an accurate digital phantom is a challenging task. This section discusses the preparation of two digital phantoms that specifically address equiaxed single phase polycrystalline materials and the steps associated with sampling and reconstructing them.

To prepare the 9 and 41 region models as phantoms, two implicit (voxel based) simulated materials models are created using *mbuilder* [4, 24, 27, 28]. *mbuilder* is the name given to a collection of software tools and reconstruction strategies developed at Carnegie Mellon University for generation of digital polycrystalline materials. In the *mbuilder* software a set of ellipsoids are packed into a volume. The ellipsoids are over packed and must be subsampled such that the final active set are those that will fill space and accurately represent the desired distributions of grain size and shape. Following the selection of the representative set of ellipsoids, the 3D model is filled with voxels using a Monte Carlo based seeded growth strategy. A seed voxel is placed at the center of each ellipsoid and then in iterative steps voxels are added to these seed points. In this way the volume of each ellipsoid in the model is filled from its centroid to its shell. As the ellipsoids are overlapping there are two intersection rules that apply. First, an ellipsoid cannot exceed its bounds. Second, when two (or more) ellipsoids share the same region in the volume, they are all permitted to claim that space in a random order. The end result is a 3D voxel structure, or image, with unique regions identified for each grain. Using a packed set of ellipsoids as opposed to a Voronoi tessellation results in a grain boundary interface structure with curvature in the grain boundaries. The added curvature is hoped to add more realism to the model; however, there is no attempt to quantify this effect. When the entire 3D region is filled with voxels, then a few steps of isotropic Monte Carlo grain growth are applied to eliminate any island voxels, or other geometric pathologies. To generate the 9 and 41 region phantoms, the parameters of *mbuilder* are set to generate an equiaxed grain morphology. The grain size and shape distributions were not selected to represent any particular real microstructure. We accept the variations provided by *mbuilder*, and rely on the generated distributions of volume, surface area and mean width to be sufficient for testing our reconstruction algorithms.

As mentioned previously, the output of *mbuilder* is an implicit representation of a polycrystalline material. The explicit geometries of the 9 and 41 region phantoms are created

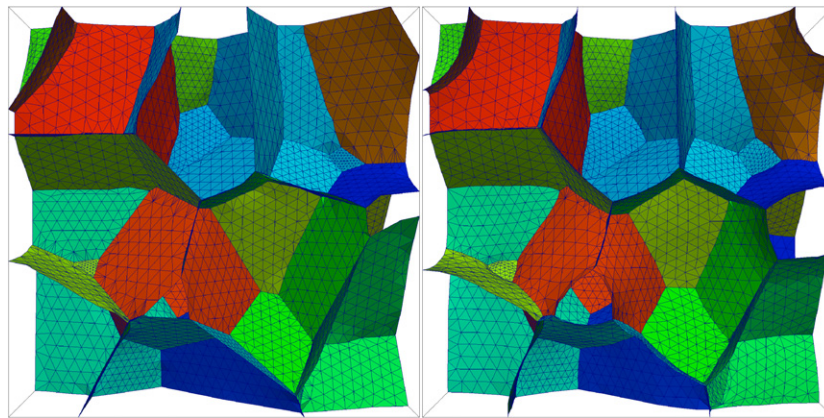


Figure 1. A side-by-side comparison of the 41 region test model before (left) and after (right) application of unconstrained MFEM. Additional curvature can be seen in both the triple lines and interfaces.

using the dual grid reconstruction algorithm [27]. The dual grid algorithm first identifies the quad points of the 3D implicit microstructure and it then proceeds to use the dual grid of the image to connect and deform the triple lines that connect the quad points. Following triple line connectivity the grain boundary patches are triangulated and the result is an explicit geometric reconstruction of the implicit polycrystalline material. The final step in phantom preparation is to evolve the interface network using a curvature based moving finite element method (MFEM) [16]. MFEM is an optimization scheme that minimizes local curvature. In an iterative manner it will move the nodes of the mesh so that the curvature between portions of the mesh is eliminated. This has a unique effect on triple lines and quad points. These unique locations in the microstructure mesh represent edges and corners and therefore are the largest contributors to local curvature because they represent the intersection of multiple surfaces. If they are allowed to move without constraint, then they will quickly contract, and will actually move more quickly than those points on the surfaces (grain boundaries). The effect that this will have on a cube will be a rapid rounding of the corners and edges. Allowed to continue, the cube would become a sphere. As a result, the unconstrained evolution of the 3D microstructure will minimize local curvature but may also increase curvature in portions of the phantoms. The result is that there is increased global curvature at the grain boundaries. MFEM was applied to the phantoms and the triple lines and quad point vertices were allowed to move freely. This freedom is needed to allow the node locations in the phantoms to be defined by real numbers as opposed to the integer values that they defined by during geometry extraction.

Figure 1 shows a side-by-side comparison of the 41 region model before and after smoothing with unconstrained MFEM. The image in the left panel of figure 1 is the original model and the image in the right panel is the evolved model. In the image on the right, additional curvature can be seen in both the triple lines and the interfaces. The image on the right is the 41 region phantom used in this study. Unconstrained evolution of the 9 region model produced similar results.

The purpose of the analysis of the geometry extraction procedure is to determine the influence of resolution on the accuracy of the reconstruction methods. To quantify the accuracy of the reconstruction, three region-based and two topology-based quantities are evaluated. The three region-based quantities are volume, surface area and mean width. The two topology-based quantities are triple line length and quad point location. Resolution is defined as the

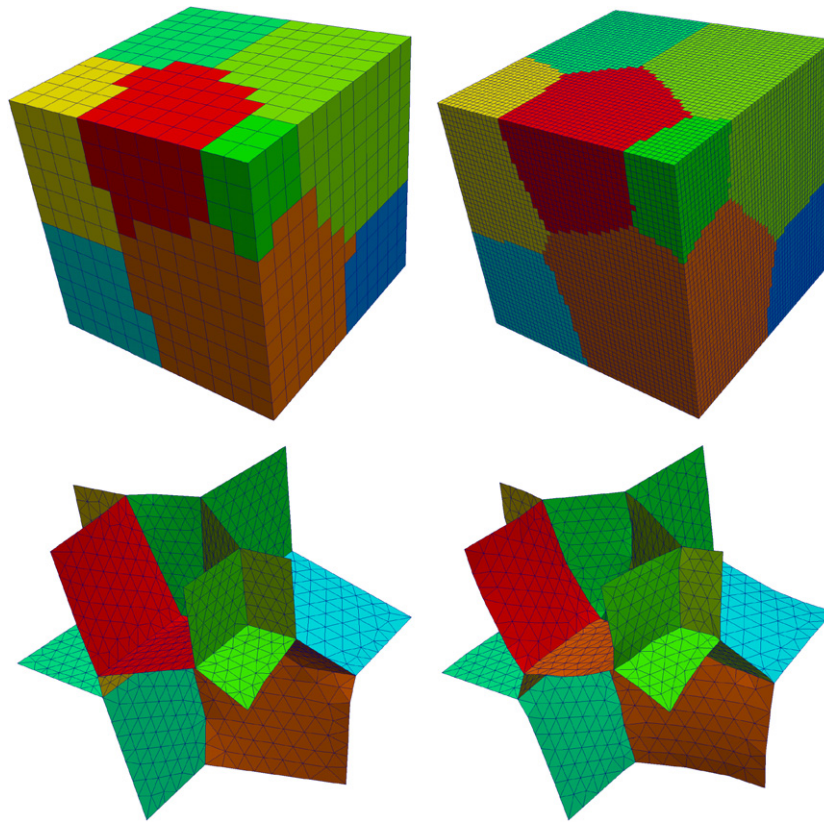


Figure 2. In the upper left is the result of sampling the 9 region model with a resolution of 12 and on the upper right is the result of sampling the same with a resolution of 50. Below each sample are the extracted geometries.

number of voxels along an edge of a model cube, i.e. a resolution of 20 indicates that the sampled model has the dimension of $20 \times 20 \times 20$ voxels. Both the 9 region and 41 region phantom geometries are cubes and they each were sampled with increasing resolution. For the 9 region model the resolution span is 11–100, or $11 \times 11 \times 11$ – $100 \times 100 \times 100$, and for the 41 region model the resolution span is 12–95.

At each resolution, an implicit representation of the phantom model is generated (i.e. a voxelized image), and for each implicit model a geometry extraction was attempted. No data cleaning procedures were used on the implicit data generated from the phantoms. A majority of the implicit data sets obtained from sampling were successfully reconstructed, but there were some failures. The reason for the failures were not analyzed in detail but they are thought to be related to quad point voxels with a small number of similar grain IDs, or in other words a dangling voxel. The sampling of the 41 region model terminates at resolution 95 rather than 100 because of the failure of the final five reconstruction attempts. Additionally, a successful reconstruction does not always indicate a pathology-free model. There are triple line loop geometries that, when presented to the reconstruction algorithms, cause the stitching of the grain boundary surfaces to introduce pathologies. These failures in robust triple line loops are thought to be related to the dangling voxel. Other potential pathologies include flipped triangle normals, zero area faces and duplicate nodes. The results presented in the next section include all successful geometry extractions, including those with pathologies.

Figure 2 shows the results of sampling the 9 region model at resolution 12 and at resolution 50. It also shows the respective reconstructions. By inspection, it is easy to see that the surfaces and triple lines at resolution 12 have much less curvature than those at 50. A comparison also shows that the locations of the quad points vary from one resolution to the next.

For each region in each *successful* geometric reconstruction, the volume, surface area and mean width are computed and written to a summary file for the reconstructed geometry. The length of each triple line, the location of each quad point, and their appropriate topological information are also written to the same file. For example, when printing a triple line length, the regions that define the triple line are also printed, and when printing a quad point location, the regions that define the quad point are also printed. The result is that each reconstructed geometry is accompanied with a file delineating the relevant statistical entities. The fitness of each reconstructed geometry can then be determined by directly comparing the entities of the reconstructed geometries with the same topological entities of the phantom geometry.

3. Results and discussion

Analysis of the accuracy of the reconstructed geometries proceeds by first looking at the total error in region quantities (volume, surface area, mean width) as a function of increasing resolution. In computing the total error at a specific resolution, these errors are summed over all regions. The total error analysis is then followed by examining the distribution of the percentage of error in each region at each resolution. Minimum, maximum and average quantities are examined as well as histograms. These are followed by analysis of error in the quad point locations and the triple line lengths. The error analysis ends by examining the error as a function of the size of the region or length of the triple line.

In computing the error analysis of the regions, the quantities of volume, V , surface area, A , and mean width, L , are defined such that

$$\begin{aligned} V &= \sum_{i=0}^{N_{\text{tet}}} V_i^{\text{tet}}, \\ A &= \sum_{i=0}^{N_{\text{tri}}} A_i^{\text{tri}}, \\ L &= \frac{1}{2\pi} \sum_{i=0}^{N_{\text{edge}}} \ell_i^{\text{edge}} \beta_i^{\text{edge}}. \end{aligned} \quad (1)$$

In equation (1) N_{tet} is the number of tetrahedra formed by joining the three nodes of a surface triangle to the centroid of the region, V_{tet} is the volume of a tetrahedron, N_{tri} is the number of triangles on the surface of a region, A_{tri} is the area of a triangle, N_{edge} is the number of edges in the surface mesh of a region, ℓ_{edge} is the length of an edge and β_{edge} is the turning angle of an edge [30].

Errors for the region quantities are normalized according to the bulk geometry of the phantom model. For example, if the phantom model is a, b, c units on a side, then the normalizing quantities would be

$$\begin{aligned} \bar{V} &= abc, \\ \bar{A} &= 2ab + 2bc + 2ac, \\ \bar{L} &= a + b + c, \end{aligned} \quad (2)$$

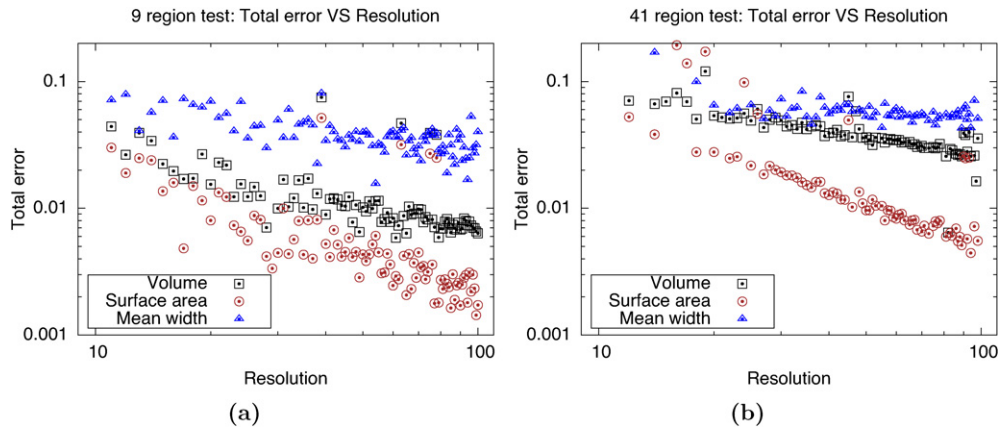


Figure 3. The total error for V , A and L are shown as a function of resolution for both the 9 region and the 41 region models. The errors of both models are similar in magnitude with the 9 region errors being lower than the 41 region errors. There are some spurious points in both data sets related to errors of the reconstruction process.

where \bar{V} is the total volume, \bar{A} is the total surface area and \bar{L} is the total mean width. The reconstruction process ensures that the final dimensions of the phantom and the reconstructed geometries are the same. Therefore, the values of \bar{V} , \bar{A} and \bar{L} for all reconstructed models are the same as their respective phantoms.

3.1. Total error analysis

The total error, $\langle \cdot \rangle_{\text{total}}^{\text{error}}$, of the region quantities, where $\langle \cdot \rangle$ is any of V , A , or L , in a reconstructed model can then be expressed as

$$V_{\text{total}}^{\text{error}} = \frac{1}{\bar{V}} \sum_{i=1}^N |\tilde{V}_i - V_i|. \quad (3)$$

The additive property of volume and area is intuitive; the fact that mean width is additive (with allowance for intersections) was established by Hadwiger [13]. In equation (3) \tilde{V}_i is the volume of the i th region of the phantom model, V_i is the volume of the i th region of the reconstructed model, N is the total number of regions and \bar{V} is the volume of the entire model and is used as a normalization of the total error. The total error is a sum of the error in all reconstructed regions and is a measure of the average accuracy of the reconstruction methods.

Figure 3 shows the analysis of the total error as defined in equation (3) for each of V , A and L as a function of resolution. The 9 region results are in figure 3(a) and the 41 region results are in figure 3(b). The total error for both phantoms for all measures decreases as resolution increases. The total error of the 9 region model is lower than that of the 41 region model, but the respective orders of magnitude of the errors are similar. In both data sets there appear to be some data points that are far away from the average results. This extreme variation is attributed to pathologies that occurred during reconstruction. Identification of the specific pathologies of the data sets that exhibit this variation has not been attempted and so the data are included in the results for completeness.

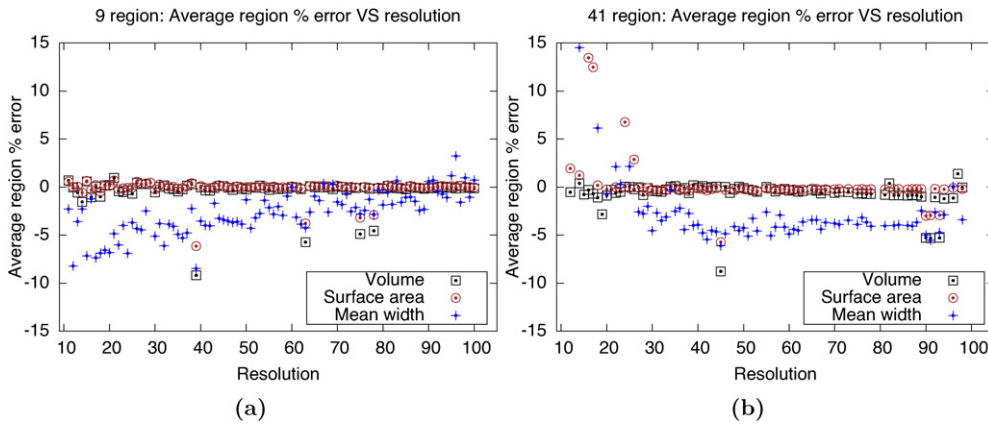


Figure 4. The average region per cent error for V , A and L are shown as a function of resolution for both the 9 region and the 41 region models. The volume and surface area errors for both models are very modest even at low resolution. They are also very tightly clustered around zero. For L , the error is clearly biased towards an under estimate, and the variation of the error does not seem to diminish with increased resolution. For the 9 region model L approaches zero error near resolution of 100, but this is less obvious for the 41 region model.

3.2. Region per cent error versus resolution

Instead of looking at total error of the entire reconstructed model, we can compute the per cent error of V , A and L for each reconstructed region. The per cent error of the i th region, $\langle \cdot \rangle_i^{\%}$, can be written as

$$\langle \cdot \rangle_i^{\%} = \frac{\langle \cdot \rangle_i - \tilde{\langle \cdot \rangle}_i}{\tilde{\langle \cdot \rangle}_i} \times 100. \quad (4)$$

In equation (4) $\langle \cdot \rangle$ can be replaced with V , A or L . A negative result in equation (4) indicates that the reconstructed model underestimated the true value and conversely a positive result indicates that the reconstructed model overestimated the true value. Consideration of the distributions of per cent error per region helps to further understand the accuracy of the reconstruction models.

From equation (4) the average per cent error per region can be determined at each resolution as well as the minimum and maximum values. Figure 4 shows the average region per cent error for the 9 region (on the left) and the 41 region (on the right) models. The volume and surface area errors for both models start rather noisy, and then quickly cluster tightly around zero. In the 9 region model this trend continues out to higher resolution, but in the 41 region model the errors exhibit larger scatter. The mean width values for both the 9 and 41 region reconstructions seem to underestimate that of the true value across all resolutions. In the 9 region model it is clear that this error moves toward zero with increasing resolution, but in the 41 region model this trend is less prominent.

The per cent error associated with each reconstructed region is evaluated according to equation (4), and the minimum and maximum errors of all the regions can also be resolved at each resolution. Figure 5 is an array of images that shows the minimum and maximum error values along with the averages. The results in column (A) of figure 5 apply to the 9 region model and the results in column (B) of figure 5 apply to the 41 region model. The y-axis of all the plots is limited to $\pm 25\%$ to enable comparison between data sets, and to emphasize the trends of the average errors. Setting the y-axis range in this way limits the field of view for the larger error bars, particularly for the 41 region volume per cent error plot. The subplot in

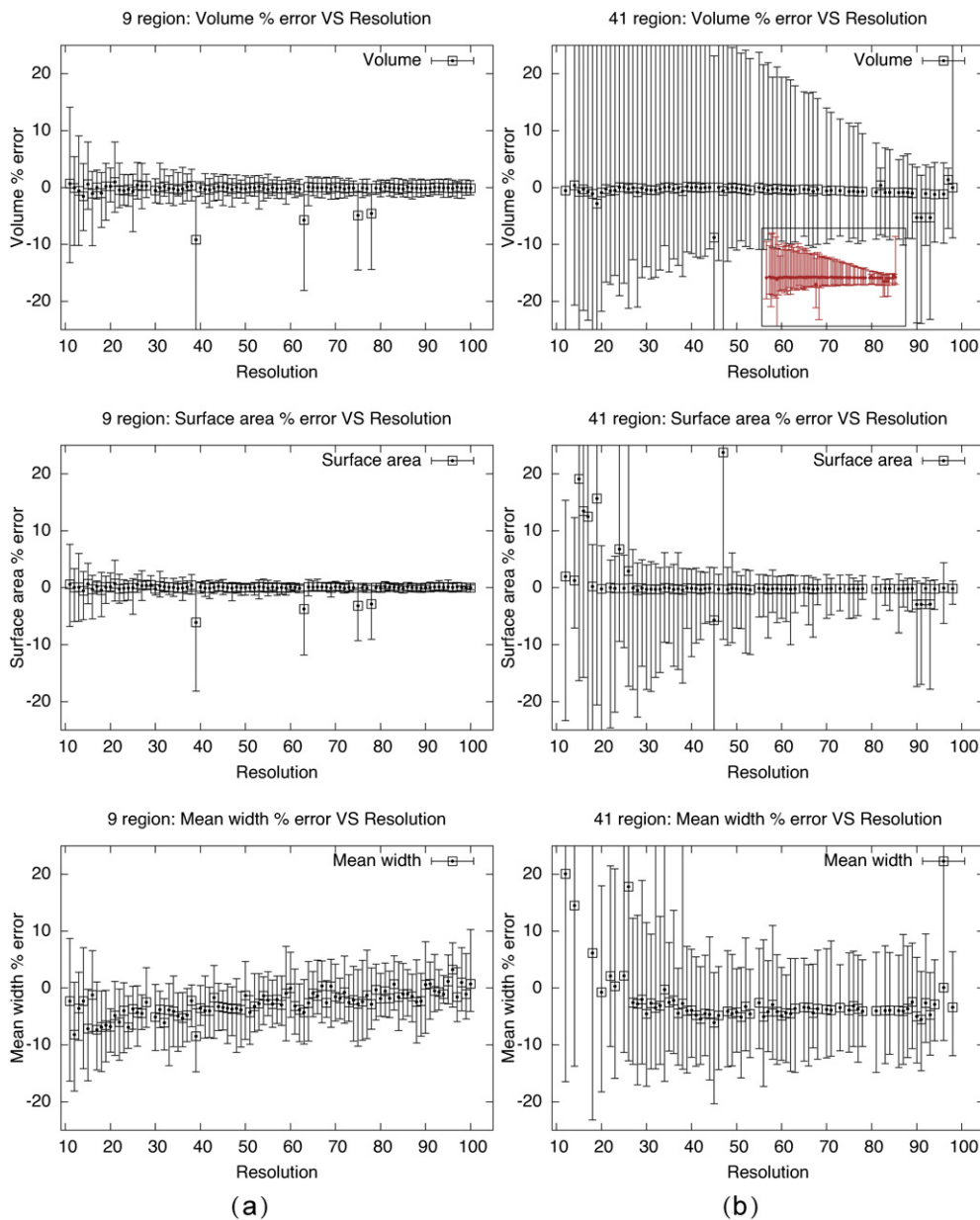


Figure 5. The minimum, maximum and average values of the region per cent error for volume, surface area and mean width are shown for the 41 and 9 region models. (a) shows the 9 region results and (b) the 41 region results.

the first row figure 5(b) shows a view of the entire data range of the 41 region volume per cent error. The y-axis range in the subplot is set to $\pm 60\%$ and the x-axis range is the same as the main plots.

In each geometric measure (V , A and L) the error bounds of the per cent error per region for the 9 region model are narrower than those of the 41 region model. The error bounds for the 41 region volume are the largest, and the error bounds for the 9 region surface area are the

smallest. With the exception of the mean width measures, the average error in all the plots is very near zero. Again with the exception of the mean width measures, the error bounds in all of the plots decrease with increasing resolution.

Looking specifically at the volumetric errors in top row of figure 5, we can see that the error in both models is centered around zero and the bounds on the minimum and maximum error are narrowing as a function of resolution. This trend applies to both the 9 and the 41 region phantoms.

Looking at the surface area errors in the second row, we see again that the average error is very near zero and that the bounds are narrowing with increasing resolution. The surface area per cent error is the most accurate and has the least variation of the three measures, and this also appears to hold for both phantoms.

Finally, looking at mean width errors in the bottom row, we see a deviation in the trends observed for the volume and surface area errors. Specifically the average per cent errors in both models are systematically below zero. In the 9 region model the error moves toward zero with increasing resolution, but this trend does not appear as strongly in the 41 region data. The second deviation that is observed is that the bounds on the mean width error are not nearly as sensitive to increasing resolution as the other metrics. The bounds on per cent error of mean width do not decrease with increasing resolution.

The persistence of the mean width error across all resolutions indicates that the geometry extraction techniques presented in [27] are not capable of modeling mean width accurately. Recall that mean width is a measure of curvature (see equation (1)); therefore the mean width errors in the bottom row of figure 5 suggest that there is a limitation of the reconstruction methods for capturing curvature accurately.

There are likely two factors in the reconstruction strategy that contribute to this deficiency. First, minimizing curvature is fundamental to the definition of using the dual grid polygon to model 3D triple lines. In [27] the authors describe a procedure to define a triple line using the dual grid polygon such that the algorithm will draw the longest line segment possible given the constraints imposed by the dual grid polygon. In other words, the procedure seeks to draw the triple line network such that it has the least amount of curvature. Second, minimizing curvature is fundamental to MFEMs employed as part of the grain boundary surface reconstruction procedure in [27] such that the optimization algorithm will seek a solution with minimum local curvature. However, in contrast to the application of MFEM to the phantoms as described in section 2, the application of MFEM to the reconstructed geometries has fewer iterations, and the locations of the triple lines and quad points are *constrained* to not move. As a result, the grain boundary surfaces are now pulled tight between the fixed triple lines. The justification for not allowing the triple lines and quad points to move, is that the dual grid provides a clear bounding envelope to their location, and allowing them to move would almost certainly cause them to violate this bounding envelop. Both of these processes attempt to minimize curvature and therefore they lead to a systematic underestimation of the mean width.

To a limited extent, increasing the resolution will increase the accuracy of the reconstruction through increasing the accuracy of the curvature of the triple lines. This effect is qualitatively observed in the upper row of figure 2 where the curvature of triple lines in the model at resolution 50 (shown on the right) are better preserved when compared with the curvature of the triple lines in the model at resolution 12 (shown on the left). However, there are many more line segments and nodes on the grain boundary surfaces than on the triple lines, and therefore the results of MFEM will have the greater impact on minimizing the grain boundary interface curvature. Without including additional information in the MFEM process the unconstrained motion of all the grain boundary surface nodes will continue to minimize curvature without respect to geometry.

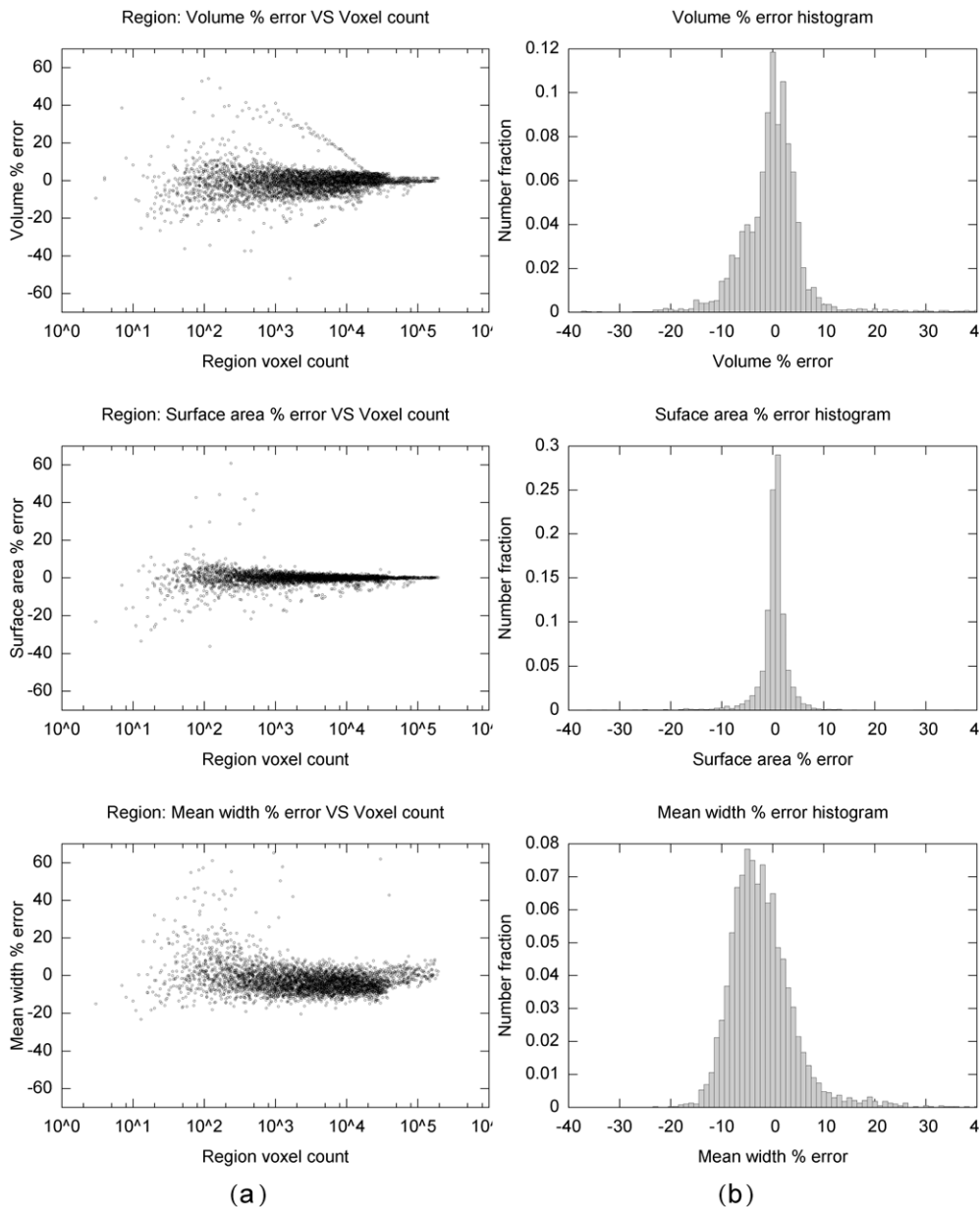


Figure 6. The plots in column (a) show the per cent error of volume, surface area, and mean width based on the number of voxels to represent a region. (b) shows the distribution of the data in column (a). The data in these plots are combined for all resolutions for both the 9 and the 41 region models.

3.3. Region per cent error versus voxel count

Another way to look at the influence of resolution is to compare the per cent error per region as a function of the number of voxels in a region. The plots in column (a) of figure 6 show the per cent error as a function of the number of voxels in a particular region. At each resolution,

a region in a phantom model is represented by a specific number of voxels, and the plots in figure 6(a) show the per cent error as a function of this number. The plots in column (b) of figure 6 show the distribution of the values from column (a). The plots in figure 6 were generated by combining the data for all resolutions of both the 9 and the 41 region models. This combined data set represents approximately 4000 regions. The smallest number of voxels to represent a region is 3 and the largest is 193903. The lower voxel counts are dominated by the data from the 41 region model and the higher voxel counts are dominated by data from the 9 region model. In both models the regions are relatively equiaxed and therefore the average number of voxels per region in the 9 region model is approximately 4.5 times that of the 41 region model.

The value of plotting the combined data in this format is that it demonstrates the specific relationship between the error of a region and the number of voxels to describe the region. The number of voxels is a dimensionless quantity and consequently the results in figure 6 are an indication of how well the reconstruction methods will reconstruct a specific object regardless of its true dimension.

In figure 6(a) the same trends are evident in the combined data as in the separated data in figure 5. The volume and surface area errors for specific regions decrease as the number of voxels to represent a region increases. Additionally, the mean width error is consistently lower than zero.

In figure 6(b) the distribution of errors is shown, and we can see that the volume error and the surface area error are indeed centered round zero, while the mean width error distribution is shifted below zero. The average per cent error for volume, surface area and mean width are -0.63% , -0.15% and -2.25% , respectively. The standard deviations are 6.67% , 3.76% and 8.04% , respectively. This supports the previous observation that surface area is the most accurate followed by volume and then mean width.

3.4. Quad point location error analysis

Error analysis of topological entities is also possible, and the triple lines and quad points are analyzed as well. For the quad points, the goal is to determine how well the location of the quad points in the reconstructed model match those of the phantom. The procedure for computing the quad point error begins with comparing the topological information of the quad points in the phantom with the topological information of the quad points in the reconstructed model. Each quad point in the phantom model is defined by the regions that intersect to form it. To determine the error of an individual quad point, a search for the matching topological entity is conducted based on the regions that define the point. For example, if regions 4, 2, 9 and 7 define a quad point in the phantom, then the error analysis will only proceed with a quad point in the reconstructed model that is defined by the same region set. When the regions of a phantom quad point are found to match the regions of a reconstructed quad point, then error is computed in the following way

$$QP_{\text{error}} = \frac{[(x_r - x_p)^2 + (y_r - y_p)^2 + (z_r - z_p)^2]^{1/2}}{\bar{L}}, \quad (5)$$

where the subscript p is for phantom, subscript r is for reconstructed and \bar{L} is the mean width of the entire model as defined in equation (2).

The results of this error analysis is seen in figure 7 where it shows the error of the location of the quad points as a function of resolution. The data in figure 7 are combined for the 9 region and the 41 region phantoms at all resolutions. The black dots and black line represent the 9 region data, and the brown dots and brown line represent the 41 region data. The dots represent

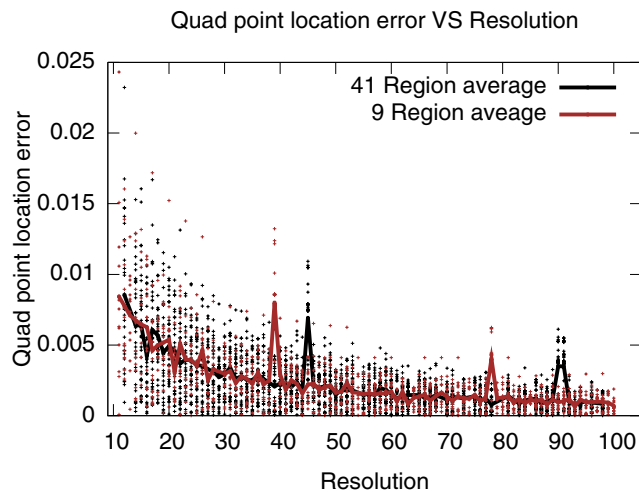


Figure 7. The error in the location of the quad points for the 9 and 41 region phantoms are shown. The solid dots and line represent the 9 region data and the average of the 9 region data, and the brown dots and line represent the 41 region data and the average of the 41 region data, respectively. The average error as a function of resolution for both the models is nearly identical.

the error for an individual quad point and the lines represent the average at each resolution step. The results for both phantoms are essentially identical, with the exception that there are many more quad points in the 41 region data. The error for both approaches zero, but does not reach it. This can be expected given that the reconstruction process will always truncate the coordinates of the quad points to integer values, whereas the location of the phantom quad points generally are not integer multiples of the voxel size. The peaks in the results in figure 7 appear to be from pathologies in the reconstruction process.

3.5. Triple line length error analysis

For the triple lines the goal is to measure the error in the length of a reconstructed triple line when compared with the topological equivalent in the phantom. The process of computing the triple line error is very similar to computing the quad point error, where the regions that define each triple line are used to match triple lines in the phantom and the reconstructed models. The lengths of the matched lines are then compared and the per cent error of the reconstructed triple line is recorded. The error analysis does not account for individual line segments but rather the sum of all lines of the same topology. For example, if there are two unique triple lines that are defined by the same three regions, but they are not connected, then these are combined into one length.

Figure 8 shows the results of the error analysis for the triple line length. In figure 8(a) the results for the 9 region triple lines are shown, and in figure 8(b) the results for the 41 region triple lines are shown. These plots are box plots and there are five values of interest at each resolution. The middle line is the median of the data, the lower bound of the box is the 25th percentile line, the upper bound of the box is the 75th percentile line, the lower whisker is the 9th percentile line and the upper whisker is the 91st percentile line. These plots illustrate that the distribution of error is contracting towards zero as a function of resolution. The mean error for triple line length approaches zero for both phantoms.

The shape of the error curves for the quad point error in figure 7 and the triple line error in figure 8 are similar. One explanation for the correlation of the triple line error to the quad

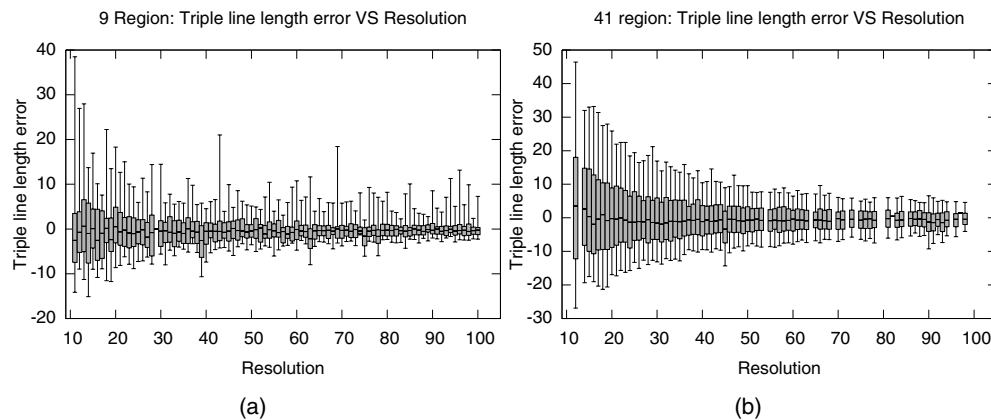


Figure 8. (a) shows the error distribution for the triple line length as a function of resolution for the 9 region model and (b) shows the same for the 41 region model. In these box blots there are five values of interest depicted for each resolution. The center line of each is the median of the data, the upper bound of the box is the 75th percentile line, the lower bound of the box is the 25th percentile line, the lower bound whisker is the 9th percentile line and the upper bound whisker is the 91st percentile line. These plots indicate that the distribution of error is contracting towards zero as a function of resolution.

point error is that the triple line length depends on the accuracy of the location of the quad points at which the line terminates. Therefore, the error, and the reduction in error of the triple line length, is coupled with the error, and reduction of error, in the quad points location.

3.6. Size of entity error analysis

To explore the effect of entity size on error we plot the size versus error. For each region or triple line a true length is defined in the phantoms, and this can be normalized by the appropriate values. The volume of each region is normalized by \bar{V} , the surface area of each region by \bar{A} , and the mean width by \bar{L} . The true triple line length is normalized by the \bar{L} of the respective phantom. Figure 9 displays the *median* of per cent error for regions and triple lines as a function of the normalized size of the regions and triple lines, and figure 10 shows the *range* of the error for the same. The 9 region and 41 region data are again combined in each of the plots, but this time they are plotted with different symbols and colors. The per cent error range for each of the plots is the range between the 9th and 91st percentile error values for each entity. This range was selected as it eliminated outliers that are likely associated with pathological errors in the reconstructed geometries.

In figure 9(a) the volume error is shown. The volume of each region in the 9 and 41 region data is normalized by the total volume of the respective phantoms. The volume fractions of the 9 region data are generally larger than those of the 41 region model. The data are sparse, but it appears that, for both phantoms, larger grains have lower error when reconstructed, and that the error is centered around zero. Figure 10(a) also shows that the range of the volume error decreases with larger grains. These results are consistent with the trends observed in figure 6, which indicate that the more voxels that represent a region the lower the spread of the volume error.

Figure 9(b) shows the median of the surface area per cent error as a function normalized surface area for both the 9 and 41 region models. The surface areas for each region are normalized by their respective phantoms. The normalized surface areas for the 9 region data

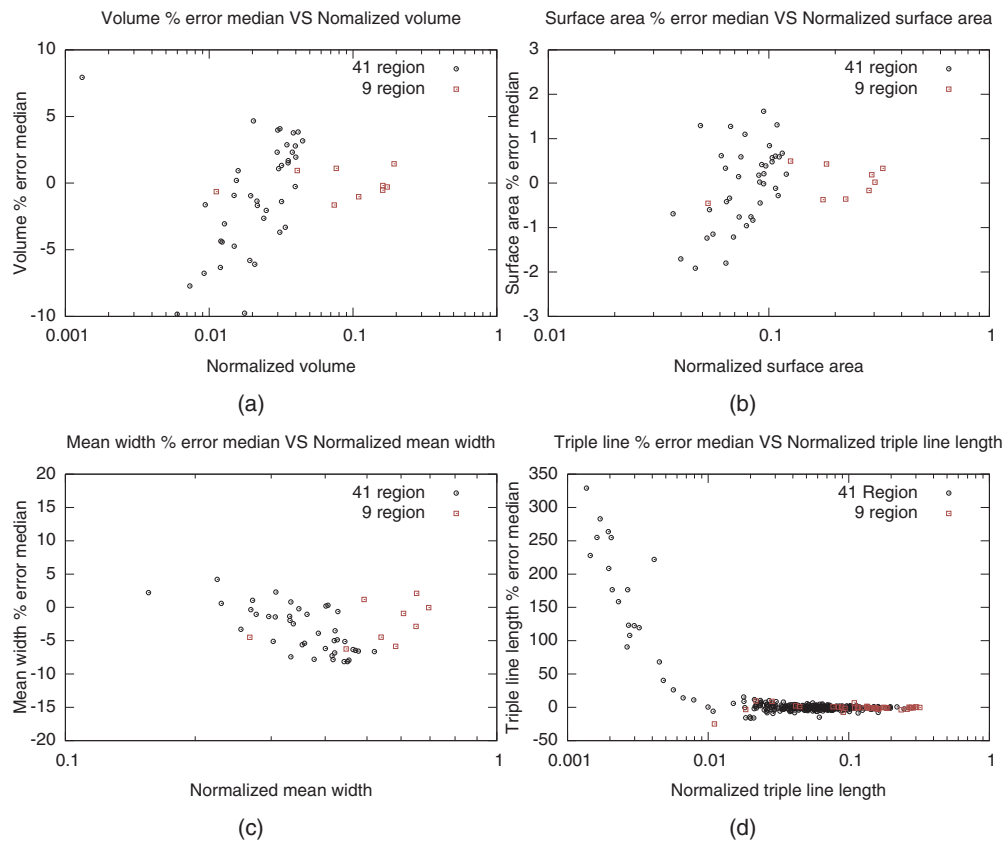


Figure 9. (a) shows the *median* of volume per cent error for each region in the 9 and 41 region phantoms as a function of the normalized size of the region, (b) shows the *median* for surface area, (c) shows the *median* for mean width and (d) shows the median for triple line length.

are again somewhat larger than the 41 region data, and the trend is that the spread of the error decreases with increasing normalized surface area. This error is also centered around zero. In figure 10(b) the range of the surface area error is shown that also decreases with increasing surface area. Again, this is consistent with the data in figure 6.

The median of the mean width per cent error for both the 9 and the 41 region phantoms are shown in figure 9(c). In this case there does not seem to be a correlation between the mean width error and the normalized mean width. That the mean width of the reconstructed geometry generally underestimates the true value is evident in this analysis as well and is consistent with the data in figure 6. In figure 10(c) the range of the mean width error is shown, which has no obvious correlation with the normalized mean width of the regions.

The triple line length median per cent error is shown in figure 9(d) for both the 9 and 41 region model data. Each triple line in the phantoms is normalized by the mean width of the respective phantom. The combined number of triple lines in both phantoms is 372, which is slightly over seven times the number of regions in the combined models. This larger population helps in the analysis of the relationships in figures 9(d) and 10(d). The median of the triple line length error shows a very strong inverse correlation with normalized triple line length. Additionally, figure 9(d) shows that very small triple lines have the highest median error, and the reconstructions always overestimate the length of the small triple lines. Figure 10(d) shows

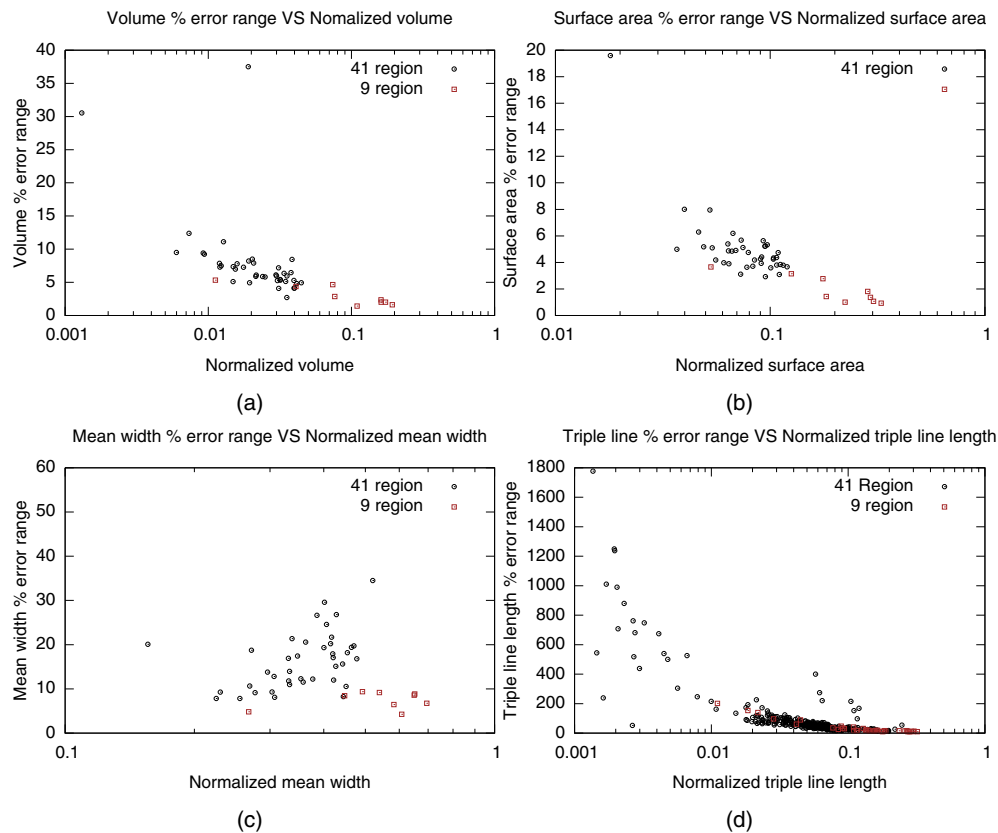


Figure 10. (a) shows the *range* of volume per cent error for each region in the 9 and 41 region phantoms as a function of the normalized size of the region, (b) shows the *range* for surface area, (c) shows the *range* for mean width and (d) shows the *range* for triple line length.

that the range of error for the triple lines also has a strong inverse correlation with the triple line length.

4. Conclusions

This study focuses on quantifying the ability of a specific algorithm [27] to reconstruct microstructures using digital phantoms. The 9 and 41 region phantoms are sampled at increasing resolution, reconstructed, and the errors associated with each reconstruction is determined. The errors are computed both for region and topological entities. The errors are normalized and the normalization is sufficient for comparing the errors from one phantom to the other.

In the total error analysis, where the error for all regions is summed, the trends in error for V , A and L decrease monotonically for both phantoms. This supports the expectation that higher resolutions provide more accurate reconstructions.

The error analysis per grain results also show a decrease in the spread of the distribution of the error as resolution increases. For the V and A errors the average error was essentially zero, but for the mean width error it was biased lower than zero. The reconstructed microstructures consistently underestimated L . This is attributed to the used of curvature minimization to smooth surfaces as a final step in the geometric modeling procedure.

The quad point and triple line errors exhibit similar trends as the region errors. The error for each and the distribution in error for each reduces as resolution increases.

The size of entity error analysis is very similar to the voxel per region error analysis and the results provide a similar guide to setting up microstructure observations. In general, the larger the entity is the less error that it has at all resolutions. And the larger an entity is, the less spread in error it has at all resolutions.

An outstanding question remains of the influence of the number of nearest neighbors on the errors in the reconstruction process. One additional explanation of the consistently lower error in the reconstruction of the 9 grain phantom may be related to the fact that on average these grains share fewer neighbors than those in the 41 grain model. That errors will occur at the interface between grains is known, and therefore a grain with fewer neighbors will therefore have less probability for error. In future work the data analysis of the reconstruction algorithms will include the ability to plot the error versus the number of nearest neighbors.

Characterizing the geometric reconstruction strategy is key to the using these methods for the analysis of 3D microstructures. The results show that there are some weaknesses in the implemented reconstruction strategy. They show that minimizing curvature has an adverse effect on the accuracy of L in the reconstructions. It is critical that the researcher is aware of this deficiency before analyzing 3D data with these tools. On the positive side, the results provide a direct guide to setting up microstructure observations, and they provide clear relationships between error distributions and resolutions. They allow the researcher to make informed decisions to balance the resolution of the data collected and the available resources.

The value of 3D microstructure data is increasing, as is the ability to collect such data. Accurate geometric reconstruction algorithms will play a key element in the scientific exploration process by enabling new visualizations and interpretations of real materials in 3D. Observations based on these data will only be as good as the 3D reconstruction algorithm allows, and therefore the performance of each algorithm should be quantified. Digital phantoms will play a critical role in the design and validation of 3D geometric reconstruction algorithms. These phantoms provide a gold standard, and a means for quantitative evaluation of algorithm performance. The phantoms used in this study can be obtained from the TMS Materials Atlas.

Acknowledgments

This work is partially sponsored by the Defense Advanced Research Projects Agency under contract HR0011-04-C-0003. Dr Leo Christodoulou is the DARPA Program Manager. Additionally it is supported under Los Alamos National Laboratory's Laboratory Directed Research and Development program. The authors are pleased to acknowledge extensive technical discussions with members of the Northrop Grumman Structural Integrity Prognosis program, particularly Drs Elias L Anagnostou and the late John M Papazian.

References

- [1] Bloomenthal J and Ferguson K 1995 Polygonization of non-manifold implicit surfaces *Proc. 22nd Annual Conference on Computer Graphics and Interactive Techniques (Los Angeles, CA, 6–11 August 1995)* ed R Cook (New York: ACM SIGGRAPH) 309–316
- [2] Boltcheva D, Yvinec M and Boissonnat J D 2009 *Medical Image Computing and Computer-Assisted Intervention 2009* (Berlin: Springer) pp 283–90
- [3] Bouman C and Sauer K 1993 *IEEE Trans. Image Process.* **2** 296–310
- [4] Brahme A, Alvi M H, Saylor D, Fridy J and Rollett A D 2006 *Scr. Mater.* **55** 75–80
- [5] Brahme A, Fridy J and Rollett A D 2007 *Materials Science Forum* **558–559** 1057–61
- [6] Chen C C, Wan Y L, Wai Y Y and Liu H L 2004 *J. Digital Imaging* **17** 279–84

- [7] Collins D L, Zijdenbos A P, Kollokian V, Sled J G, Kabani N J, Holmes C J and Evans A C 1998 *IEEE Trans. Med. Imaging* **17** 463–8
- [8] Dillard S E, Bingert J F, Thoma D and Hamann B 2007 *IEEE Trans. Vis. Comput. Graph.* **13** 1528–35
- [9] Gedamu E L, Collins D L and Arnold D L 2008 *J. Magn. Reson. Imaging* **28** 308–19
- [10] Goodenough D J and Weaver K E 1988 *Comput. Med. Imaging Graph.* **12** 193–209
- [11] Guangzhi C, Bouman C A and Webb K J 2006 *40th Asilomar Conf. on Signals, Systems and Computers, 2006. ACSSC '06 (Pacific Grove, CA)* pp 156–60
- [12] Guangzhi C, Bouman C A and Webb K J 2009 *IEEE Trans. Image Process.* **18** 2085–99
- [13] Hadwiger H 1957 *Vorlesungen über Inhalt Oberfläche und Isoperimetrie* (Berlin: Springer)
- [14] Ju T, Losasso F, Schaefer S and Warren J 2002 *ACM Trans. Graph.* **21** 339–46
- [15] Kadosh A, Cohen-Or D and Yagel R 2003 *IEEE Trans. Vis. Comput. Graph.* **9** 580–6
- [16] Kuprat A 2000 *SIAM J. Sci. Comput.* **22** 535–60
- [17] US National Library of Medicine 2011 The national library of medicine's visible human project (www.nlm.nih.gov/research/visible/visible_human.html)
- [18] Peter A M and Rangarajan A 2008 *IEEE Trans. Image Proc.* **17** 458–68
- [19] Price R R, Axel L, Morgan T, Newman R, Perman W, Schneiders N, Selikson M, Wood M and Thomas S R 1990 *Quality assurance methods and phantoms for magnetic resonance imaging: Report of AAPM nuclear magnetic resonance Task Group No. 1* vol 17 (College Park, MD: AAPM)
- [20] National Library of Medicine Board of Regents 1990 *Electronic Imaging: Report of the Board of Regents* vol 90, part 2197 (Washington, DC: US Department of Health and Human Services, Public Health Service, National Institutes of Health)
- [21] Rollett A D, Lee S B, Campman R and Rohrer G 2007 *Ann. Rev. Mater. Res.* **37** 627–58
- [22] Rollett A D and Manohar P 2004 *Continuum Scale Simulation of Engineering Materials* ed D Raabe *et al*, 1st edn (Weinheim, Germany: Wiley-VCH) pp 77–114
- [23] Rossignac J R and Requicha A A G 1991 *Computer-Aided Des.* **23** 21–32
- [24] Saylor D, Fridy J, El-Dasher B, Jung K Y and Rollett A 2004 *Metall. Mater. Trans. A* **35** 1969–79
- [25] Scheins J J, Herzog H and Shah N J 2011 *IEEE Trans. Medical Imaging* **30** 879–92
- [26] Schuh C A, Minich R W and Kumar M 2003 *Phil. Mag.* **83** 711–26
- [27] Sintay S D 2010 *Statistical microstructure generation and 3D microstructure geometry extraction PhD Thesis* Carnegie Mellon University
- [28] Sintay S D, Rollett A D and Groeber M 2009 *Electron Backscatter Diffraction in Materials Science* ed A J Schwartz *et al* 2nd edn (Berlin: Springer)
- [29] TMS 2012 *Materials atlas home* (<https://cosmicweb.mse.iastate.edu/wiki/display/home/Materials+Atlas+Home>)
- [30] Uyar F, Wilson S R, Gruber J, Lee S, Sintay S D and Rollett A D 2009 *Int. J. Mater. Res.* **100** 543–9
- [31] Wang C C L 2007 *Comput. Aided Des.* **39** 35–50
- [32] Woo D C, Choi C B, Kim S S, Rhim H S, Jahng G H, Baek H M, Nalcioglu O and Choe B Y 2009 *Concepts Magn. Reson. B: Magn. Reson. Eng. B* **35** 168–79